Testing and Life Prediction for Composite Rotor Hub Flexbeams

3rd International Conference on Fatigue of Composites
Kyoto, Japan
13-15 September 2004

Gretchen B. Murri
Research Engineer
U.S. Army Research Laboratory, Vehicle Technology Directorate, Hampton, VA
Gretchen.B.Murri@nasa.gov

ABSTRACT

A summary of several studies of delamination in tapered composite laminates with internal ply-drops is presented. Initial studies used 2D FE models to calculate interlaminar stresses at the ply-ending locations in linear tapered laminates under tension loading. Strain energy release rates for delamination in these laminates indicated that delamination would likely start at the juncture of the tapered and thin regions and grow unstably in both directions. Tests of glass/epoxy and graphite/epoxy linear tapered laminates under axial tension delaminated as predicted. Nonlinear tapered specimens were cut from a full-size helicopter rotor hub and were tested under combined constant axial tension and cyclic transverse bending loading to simulate the loading experienced by a rotorhub flexbeam in flight. For all the tested specimens, delamination began at the tip of the outermost dropped ply group and grew first toward the tapered region. A 2D FE model was created that duplicated the test flexbeam layup, geometry, and loading. Surface strains calculated by the model agreed very closely with the measured surface strains in the specimens. The delamination patterns observed in the tests were simulated in the model by releasing pairs of MPCs along those interfaces. Strain energy release rates associated with the delamination growth were calculated for several configurations and using two different FE analysis codes. Calculations from the codes agreed very closely. The strain energy release rate results were used with material characterization data to predict fatigue delamination onset lives for nonlinear tapered flexbeams with two different ply-dropping schemes. The predicted curves agreed well with the test data for each case studied.

Introduction

Polymeric composites are used extensively in the manufacture of dynamic structural components within the rotorcraft industry. One application is hingeless, bearingless composite helicopter rotor hubs, which have reduced weight and drag, as well as fewer parts, compared to metal hubs. During flight, rotor hubs are subjected to constant axial tension load from the centrifugal forces, as well as cyclic bending loads. In order to accommodate this bending, the stiffness of the flapping flexure region is changed by varying the thickness of the hub arm. This

thickness change is accomplished by dropping, or terminating internal plies in that region. However, these internal ply-drop locations create discontinuities, which are sources for delamination initiation. In order to design damage resistant tapered structures, many parameters affecting delamination at dropped plies, such as the taper geometry and location of the ply-drops through the thickness must be considered.

Several other researchers have studied delamination in linear tapered laminates with internal ply drops under pure tension loads. References 1-5 used FE modeling and stress-based failure criteria to predict the strength of tapered laminates of a variety of different materials and with different internal ply-drop configurations. In each study it was determined that high interlaminar stresses at the ply-drop locations led to delamination onset at the ply-drops. In [2, 6-8], researchers considered the influence of several parameters, such as taper angle and number of dropped plies, on the stress field near the dropped ply locations. Other investigators [9-11] used a strain energy release rate approach to study delamination in tapered laminates with axial tension loading. In [9], Wisnom compared tapered specimens with internal dropped plies to similar specimens with internal cut plies but no tapered geometry, and tapered laminates where the taper was created the inclusion of nylon films in the layups. Although there were high interlaminar normal stresses in all three configurations, delamination was controlled by the strain energy release rate resulting from the dropped plies geometry.

This paper discusses the development of a fracture-mechanics-based approach to analyzing and predicting the behavior of tapered laminates subjected to the type of combined tension-bending loading experienced by helicopter rotor hub flexbeams. In ref. 12, O'Brien proposed a damage-threshold/fail-safety approach for assessing the durability of composite structures. This approach assumes the existence of flaws such as matrix cracks or resin pockets that act as sources for delamination onset, and uses strain energy release rate characterization to predict delamination growth. This is the approach which was use in the work discussed in this paper to characterize delamination growth in tapered flexbeam laminates with internal ply-drops. The initial work considered flexbeams with constant linear taper sections, under axial tension loads, and with a variety of layups and materials. Later studies considered flexbeams with nonlinear taper sections and combined axial-tension, transverse-bending loads. Both analytical and experimental results are presented. Predicted delamination fatigue lives are compared with test data for several configurations.

Linear Tapered Flexbeams

References 13-15 considered flexbeams with linear tapered sections, such as shown in fig.1, with continuous exterior, or belt, plies; continuous interior, or core, plies; and terminated, or dropped plies, which were dropped in a

staircase pattern, in groups of two. Figure 1 shows a flexbeam with constant-thickness thick and thin sections, and a midsection with a taper angle of 5.71º. In [13-15], finite element studies were performed to evaluate the interlaminar stress distributions in such a laminate under axial tension loading. A 2D, plane-strain model of the laminate half-thickness was created, with the smallest elements having dimensions of h/4, where h is the ply-thickness. These smallest elements were used in the areas around the dropped plies, and at the juncture of the tapered and thin regions, as shown in fig. 2. Nominally triangular resin pockets have been observed at the end of the dropped plies Therefore, resin pockets at the ply-endings were modeled using triangular elements and pure resin properties. Fixed conditions were modeled at the thin end and uniform tension was applied at the thick end.

In ref. 13, a laminate with the geometry of fig. 1 was modeled using material properties for S2/SP250 glass/epoxy and an angle ply-layup of 0 and ±45 plies, where the dropped plies are ±45 pairs. Interlaminar stresses were calculated along the interface between the belt and dropped plies in the thick and tapered regions; and between the belt and core plies in the thin region (interface ABCD in fig. 1). The interlaminar normal stresses (in the local coordinate system) in fig. 3 show sharp peaks at the points of material and geometric discontinuity, e. g., at the ends of the dropped plies and at the juncture of the tapered and thin sections (points B, E, F, and C). Similar peaks were calculated at the same locations for the interlaminar shear stresses. The FE model was then modified to use isotropic material properties throughout. For that case, the interlaminar normal stresses showed no sudden changes at either the dropped ply locations, or the tapered-thin juncture. The same model was also used in ref. 14 and 15, to calculate interlaminar stresses for the same loading, but using IM6/1827I graphite/epoxy properties and a uni-directional layup (ref. 14), or S2./SP250 glass/epoxy properties and a different angle-ply layup (ref. 15). Each modeled case showed results similar to fig. 3. Therefore, these sharp stress changes were considered to be due to the material discontinuities at those locations, and the tapered geometry, rather than the material modeled or a specific layup.

Because the highest interlaminar normal stresses always occurred at the juncture of the tapered and thin sections, (point C in fig. 1), and because the stresses were tensile on both sides of C, it was assumed that in these flexbeams, under tension loading, delamination would start at point C, and grow either toward the thick or thin regions. In order to simulate this delamination growth in the FE model, multi-point constraints (MPC) were created at the nodes along interface ABCD. Delamination growth was then modeled by incrementally releasing the MPCs, and simulating a delamination of length *a*, growing from point C into the tapered region, between the belt and dropped plies (interface BEFC), or a delamination of length *b*, growing from point C into the thin region, between the belt and core plies (interface CD). See fig. 4(a). At each increment, the virtual crack closure technique (VCCT) [16]

was used to calculate the strain energy release rate, G, associated with that delamination. The VCCT calculates the individual mode components of strain energy release rate, using the forces at the delamination tip, and the relative displacements behind the delamination tip, where both are measured in the local coordinate system; i.e., the normal-tangential (n-t) coordinate system for the deformed elements.

Figure 5 shows the G results for a variety of delamination lengths in both directions away from point C. On the right side of fig. 5, G values are shown for delaminations growing a distance *b* along interface CD, with delaminations of a fixed length *a* (*a*=0, 6h, 12h, or 24h) modeled on interface CB. Similarly, on the left side of the figure, G values are shown for delaminations growing distance *a* along interface CB, with delaminations of a fixed length (*b* =0, 6h, 12h, or 24h) modeled on interface CD. As shown in the right side of fig. 5, as delamination *b* grew, G increased very quickly and reached a peak and then remained at a plateau or dropped slightly. Similar behavior was observed on the left side of the figure, where sharp peaks in G appeared where the delamination reached the dropped plies at points F and E. These G calculations were repeated in ref. 14 and 15, substituting the materials and layups used in those studies in the FE model. The observed pattern was the same. For delamination from point C, in either direction, G quickly reached a peak value and then gradually dropped. Also, for each case modeled, the peak value was always highest for delamination in the direction of the taper, indicating that for this taper geometry, delamination is likely to grow toward the tapered region first.

The fact that the calculated G value decreases after reaching a peak seems to indicate that stable delamination growth should be expected in these laminates. However, the family of curves in fig. 5 indicates that the growth is more likely to be unstable: e.g., Consider a delamination growing from point C in an undamaged laminate. Because the peak value of G in fig. 5 is higher in the tapered direction, delamination is likely to grow there first. However, delamination growth in that direction increases the calculated G for delamination in the other direction, causing delamination to now grow in the thin direction. In the same manner, that delamination increases G for further delamination growth in the tapered direction, resulting in unstable delamination growth in both directions away from point C.

In refs. 14 and 15, laboratory testing was used to study delamination in these tapered laminates under cyclic tension. Small coupon specimens with the geometry shown in fig. 1 were made from either S2/SP250 or S2/CE9000 glass/epoxy; or from IM6/1827I graphite/epoxy. In ref. 14, only unidirectional flexbeams were tested; in ref. 15, S2/SP250 specimens with an angle ply layup were tested. In each study, test specimens were cyclically loaded in tension in a hydraulic test stand, at a frequency of 5 Hz and an R-ratio of 0.1, until they delaminated

unstably. For all of the IM6/1827I and S2/CE9000 specimens, delamination began in the form of a crack behind the resin pocket at the tip of the innermost dropped ply, (point F in fig.1). As the loading continued, delaminations grew stably, from this crack through the tapered region toward the thick region, between the core and belt plies, and between the belt and dropped plies, as shown in fig. 4(b). Delaminations grew stably throughout the length of the tapered region and sometimes into the thick region. All of the S2/SP250 laminates, both unidirectional and angle-ply, failed unstably from point C, with no stable delamination growth.

The final unstable failure occurred in all the laminates along the interface between the belt and dropped plies in the tapered region (interface BC) and between the belt and core plies interface (CD) in the thin region. Figure 6 shows a close-up photo of the area around the resin pocket where the delamination initiated. The photo shows the crack behind the resin between points F and F', and the delamination around the dropped plies and in the thin region.

In ref. 14, the FE model was modified to include the initial tension crack behind the resin pocket and delamination along the interfaces above and below the dropped ply group in the tapered region, with the delamination extending as far as the tip of the outermost dropped-ply group, as shown in fig. 4(b). Strain energy release rates were then calculated for a delamination starting at point C and growing along interface *a* or *b*. Figure 7 shows calculated G values for the flexbeam with no initial delamination damage, and the corresponding results for the model with initial delamination damage (figs. 4(a) and 4(b), respectively). The results were qualitatively similar to fig. 5, although the G values for the initially delaminated case were higher, with the highest values found for delamination toward the tapered region. This pattern was observed for all three material systems modeled.

Because the strain energy release rates were calculated using VCCT, the individual mode components could be determined. Figure 8 shows the ratio of G_I to total G for delamination growth into either the thin or tapered regions. The initial delamination growth was almost completely mode I for all three materials, for delamination growth in either direction. However, delamination growth into the tapered region became primarily mode II as the delamination grew, reaching 85% mode II at a/h=20.

Non-Linear Tapered Flexbeams With Combined Tension-Bending Loading

In refs. 13-15, the effect of axial tension on linearly tapered laminates was studied using laboratory tests and analyses. However, rotor hub flexbeams are subjected to the more complex loading scheme of a constant axial tension load (due to the centrifugal forces) combined with cyclic bending loads. In addition, typical hub designs use a nonlinear taper geometry, created by a staggered ply-drop scheme.

In order to be able to apply combined tension and bending loads to coupon specimens, a hydraulic test frame, called the axial tension and bending machine (ATB) was designed and built at NASA Langley Research Center [17]. A schematic of the ATB is shown in fig. 9. As the figure shows, the axial load cell is incorporated in the top grip and rotates with the thin portion of the tapered laminate as the transverse load is applied. With the axial load applied under load control, a constant membrane load can be maintained while the flexbeam is subjected to bending under transverse stroke controlled mode. The specimens were bolted into the grips and a tension load, P, was applied first, followed by the transverse load, V.

In the following studies [18-20], a combination of experiments and FEA of nonlinear tapered laminates under combined loading was used to predict delamination onset in these laminates. A fracture mechanics methodology, using strain energy release rate values calculated from the FEA, and material characterization data, was used to calculate a curve relating maximum surface strain in the flexbeam to the number of loading cycles at delamination onset.

In ref. 18, coupon specimens cut from a full-size S2/E7T1 glass/epoxy flexbeam, as shown in fig. 10, were tested in the ATB under combined tension-bending loading. The specimens were nominally 340mm (13.4 in.) long and 25.4 mm (1-inch) wide. The specimens had a nonlinear taper and were symmetric about the midplane. The specimens were instrumented with strain gages at 4 locations along the length on each side, with one gage near the juncture of the thick and tapered regions, two in the tapered region, and one in the thin section. The specimens were placed in the ATB grips so that there was a 12.7 mm (0.5 in.) thick region, a 127 mm (5 in.) tapered region, and a 25.4 mm (1.0 in) thin region. The flexbeam layup may be visualized, as shown schematically in fig. 11, by assuming that the laminate consists of 5 continuous belt-ply groups (groups B1-B5), a continuous surface ply of woven 7781 E-glass/E7T1-2 fabric (group F), and 4 dropped-ply groups (groups D1-D4) on each side of the mid-plane. Each dropped-ply group consisted of 13 plies of differing lengths, in a non-uniform staggered staircase drop pattern, to produce the nonlinear surface contour.

The flexbeam specimens were tested in the ATB machine. Static excursions tests were done prior to fatigue testing, by applying a constant axial tension load of approximately 35.6 kN (8000 lbs) and then applying the transverse bending stroke, δ, in increments of approximately 2.53 mm (0.1 inch), to a maximum displacement of 30.5 mm (1.2 inch) and recording the surface strains at each step. Surface strains measured during the static excursion testing showed that the highest stains occurred at about 90.9 mm (3.59 in.) from the bottom grip, in the tapered region. Those strains are plotted in fig. 12, as a function of the applied transverse load, V. As the figure

shows, the relationship is linear when the axial load is held constant. This relationship was used to choose the maximum cyclic transverse stroke for the fatigue tests. Because the boundary conditions in the ATB differ from those of the full-scale flexbeam in the rotor hub, it was more logical to control the tests to a desired maximum surface strain (comparable to what a flexbeam experiences in flight), than to a prescribed transverse deflection. Therefore, the results shown in fig. 12 were used to select the maximum transverse stroke necessary to achieve the desired maximum strain level for fatigue testing.

For fatigue testing, the specimens were bolted into the ATB grips and a tension load of approximately 35.6 kN (8000 lbs) was applied. This axial load corresponded to the net axial stress due to CF in the full-scale hub. The maximum transverse load, V, was then applied by cycling sinusoidally, at a frequency of 3 Hz, using fully-reversed loading (R=-1). Loads were chosen to produce maximum surface strains, ε_{max}, of either 11000 or 10000 με. The specimens were cycled until they either failed by unstable delamination completely along the length, or reached 2 million cycles without damage (considered a run-out).

A 2D FE model of the tapered laminate was developed to duplicate, as closely as possible, the geometry of the tested flexbeams, including the non-linear taper in the specimen, and the boundary conditions of the ATB test configuration. The continuous curvature of the tapered section of the flexbeam was approximated in the model by using ten short linear taper sections, with gradually decreasing taper angles. Continuous belt-ply-groups (B) and dropped-ply-groups (D) were modeled in the analysis, using smeared orthotropic material properties from laminated plate theory for each ply-group. The loading conditions of the model duplicated the test conditions.

A schematic of the FE model is shown in fig. 13. The model consisted of four-noded isoparametric quadrilateral plane strain elements and 3-noded triangular elements, which were used to represent resin pockets at the tips of each of the eight dropped-ply groups. Each distinct ply-group was modeled using one element through the ply-group thickness. Square elements were used in belt ply-groups B2, B3, B4, and B5, in the tapered region near the thick end of the model. In order to assign the material properties correctly in the tapered region of the model, a local coordinate system was assigned to each element, with the 1-direction parallel to the element side from the local node *i* to local node *i+1*, as shown in fig. 13. The local t-n coordinate system was used to assign material properties for each element in the model.

Fixed conditions were applied at the thick end of the model to simulate clamped conditions. An axial tension load was applied at the thin end and a point load was applied in the negative Y-direction at the thin end of the model to create bending. The ABAQUS finite element code was used in the analysis, using the geometric non-linear

solution option to account for the large deflections of the flexbeam.

To determine whether the FE model can accurately simulate the behavior of the test specimens under identical loading in the ATB, the calculated surface strains were compared to the measured surface strains from the strain gages, at the maximum transverse stroke condition from the static excursion testing. Results are shown in fig. 14. The measured strains are somewhat higher than predicted at the location nearest the bottom grip, but over the rest of the specimen there was very good agreement between the test and analysis results.

Specimens were periodically inspected visually during the fatigue testing for delamination growth at the edges. Delamination always started in these specimens as a tension crack at the interface between the D4 ply-group and the adjacent resin pocket. These cracks were faint, but visible on the flexbeam surface during testing. Once a tension crack formed, delaminations grew from the crack toward the thick region, either at the interface under D4 (*a'*), along the interface above D4 (*a*), or at both interfaces simultaneously. (See fig. 15.) These delaminations grew rapidly, but stably, until they approach the juncture of the tapered and thick regions. Final unstable delamination occurred by delaminations growing unstably along the length of the specimen, including from the crack at the tip of D4, into the thin region, along interface *b*. Figure 16(a) shows a photo of a typical final failure. Figure 16(b) shows a close-up of the area around D4 where delaminations were first observed.

Multi-point constraints were used to simulate the observed delamination growth from the tests in the FE model. Because delamination was most often observed to occur first in the test specimens at the interfaces around the tip of ply-group D4 (fig. 15), MPCs were imposed at those interfaces to allow simple modeling of delaminations by releasing the MPCs. The tension crack behind the resin pocket, as well as delaminations at the interfaces *a*, *a'*, and *b*, were modeled by incrementally releasing MPCs along those interfaces. Strain energy release rates were calculated using VCCT for a delamination starting at the resin and growing either along *a*, or *a'*, with no other delaminations in the model, and for a delamination growing along *b*, but with initial delamination growth existing along *a* and *a'*. These configurations were chosen to reflect the delamination progression that was observed in the test specimens. Figure 17 shows calculated G values for four different patterns of delamination growth. On the left side of the figure, G is shown for delamination along interface *a*, with no other delamination modeled, and for delamination along interface *a'*, with no other delaminations. As the data shows, the peak value is higher for growth along *a'*, the interface under the dropped plies, implying that that is the more dominant direction for delamination onset. On the right side of the figure, G values are shown for a delamination growing from the tip of the resin along interface *b*, with two different length delaminations along interface *a'*. Results were higher for the case with the

longer value of *a'*. Together, the G results suggest that for this configuration, delamination will grow first along the interfaces around the dropped ply group (D4), all or most of the way to the juncture of the taper and thick sections, and then unstably along interface *b*, into the thin region.

The individual mode components were calculated for each of the 4 delamination configurations calculated in fig. 17. For this flexbeam, delamination into the tapered region along either *a* or *a'* was between 70 and 100 percent mode II. Delamination into the thin region along *b*, however, was 80 to 100 percent mode I.

The calculated G values were used to predict delamination onset as a function of loading cycles, using material characterization data from fatigue tests of the test material, similar to that shown in fig. 18. Each data point in the figure represents the point at which delamination growth began in a DCB specimen under (Mode I) cyclic loading [21, 22]. Although the initial delamination growth in these flexbeam laminates was shown to be mode II, G_{IImax} data was not available for this material. Previous studies, however, have shown that there may be little difference in mode I and II G vs. N data at long lives, so G_{Imax} vs. N data was used in the analysis. A curve was fit through the DCB data which had the form

$$G_{Imax} = c(N^d) \tag{1}$$

Then it was assumed that delamination would grow when the peak G from the FE calculations equaled the cyclic G for delamination onset in the DCB tests, where both G terms were normalized by the ply thickness, h, and the square of the bending load, V. That is,

$$\left[\frac{Gh'}{V'^2}\right]_{FE} = \frac{G_{Imax}h}{V^2} \tag{2}$$

The terms on the left refer to the calculated G from the FE model, with a modeled ply thickness h', and a prescribed transverse load of V'. On the right side of the equation, h is the average measured ply thickness from the test specimens and V is the bending load applied during testing. However, because these coupon tests are compared to full-scale flexbeams by relating surface strains, rather than loads, it was more useful to substitute the relation between the applied load V and the surface strains. Recall (from fig. 12) that when the axial load is held constant, there is a linear relationship between the applied bending load and the maximum surface strain, which can be expressed as

$$\varepsilon_{max} = e + fV \tag{3}$$

Substituting eqs. (1) and (3) into eq. (2) and solving for ε_{max}, gives

$$\varepsilon_{\max}(N) = e + f\sqrt{\frac{cN^{d}h}{\left[\frac{Gh'}{V'^{2}}\right]_{FE}}} \tag{4}$$

relating the number of loading cycles to the maximum applied surface strain.

The number of loading cycles to the final unstable delamination, $N_{failure}$, of the flexbeam can be considered the sum of the number of cycles necessary to create the tension crack, N_{tc}; the number of additional cycles to the onset of delamination along *a* or *a'*, N_1; the number of cycles for stable delamination growth along those interfaces, N_2; and the number of additional cycles to the onset of unstable delamination along *b*, N_3. If N_{tc} and N_2 are considered negligible, then $N_{failure}= N_1+ N_3$. Equation (4) was used to calculate curves relating the maximum cyclic bending strain and the number of loading cycles to the onset of delamination along a' (N_1), and to the final unstable delamination (N_3).

To calculate a curve showing cycles to delamination along *a'*, eq. (4) was computed using a peak G value for delamination along *a'* with *a*=*b*=0. A second curve was then calculated using a peak G value for a flexbeam with both interfaces around D4 completely delaminated and a delamination growing along interface *b*. Those two curves were added, to give the cycles to delamination onset along a' and to final unstable delamination. The resulting curve is shown in fig. 19, along with the test results at unstable delamination. The shaded area in fig. 19 represents the prediction plus and minus one standard deviation. All of the test data fall within the standard deviation, although the tendency was to slightly under-predict the cycles to failure at higher strain level, and over-predict at the lower strain level.

Reference 18 showed that simple 2D FE models could replicate the global response of coupon size flexbeam specimens under combined loading. Calculated strain energy release rates from modeled delamination growth were used with material characterization data to accurately predict fatigue lives of the test specimens compared to the test data. In ref. 19 and 20, this approach was used again for flexbeam laminates with a different ply dropping pattern, a different nonlinear geometry, and using a hybrid glass-graphite material system. Also, for these studies, two different FE analyses were used, to assess differences in the codes, and to determine what parameters have significant effects on the results of the analyses.

Test specimens from [19, 20] were cut from the outboard tapered region of full-size flexbeams on a commercial Sikorsky Helicopter tail rotor and were similar to those shown in fig. 10. The flexbeams were fabricated using a

combination of S2/8552 glass/epoxy and IM7/8552 graphite/epoxy. In contrast to earlier studies, where the plies were dropped in pairs in a regular staircase pattern [13-15]; or in groups of multiple plies, in an irregular staircase pattern [18]; these ply terminations occurred in overlapping stepped pairs of either 45/-45 plies, or 4-ply groups of $[0_2/45/-45]$, with the shorter plies of the pairs nearer the midplane and the longest plies to the outside of the specimen. Fig. 20 shows a close-up of the edge of one specimen. The figure shows the ply-dropping arrangement and the hybrid nature of the flexbeams. The ply-drop location of primary interest is labeled in the photo as 311.

All of the specimens were tested under combined tension-bending loading in the ATB. As for the previous tests, the specimens were instrumented with strain gages along the length, and were loaded statically, prior to fatigue testing, to determine the relationship between the applied loads, and the specimen transverse deflection and surface strains. Both the static and cyclic loads were applied in the same manner as in ref. 18, and described above. For these specimens, the maximum strain levels for fatigue testing were between 4500 and 8000 με. These levels represented accelerated testing rates and are not representative of component capability or typical flight conditions. To more accurately simulate the loading experienced in flight, these specimens were cycled using an R-ratio of approximately R=0.1, rather than the fully-reversed loading (R=-1) that was used in the earlier studies.

A FE model was developed that duplicated the nonlinear tapered geometry of the flexbeam and the boundary conditions of the test machine. Details of the model are given in refs. 19 and 20. The model was analyzed using both the ANSYS and ABAQUS FE codes, to evaluate the effect of differences in the way the two codes implement orthotropic material properties, constraint equations, and solution algorithms. Both codes used a 2D eight-noded plane-strain quadrilateral element with reduced integration, as well as a nonlinear solution routine with large deformation options, and surface-to-surface contact. Delamination was modeled, as in the earlier studies, by incrementally releasing MPCs at the interfaces around the ply endings.

Strain energy release rates were calculated using the VCCT, with both FE codes. Figure 21 shows the mode I and mode II components of total G from the ANSYS model for delamination from ply-ending 311, growing along each of the three potential interfaces. A comparison of the peak values along the different delamination paths indicates that delamination is most likely to grow along interface *a'*, under the dropped plies, first. The figure also shows that delamination toward the thick end of the flexbeam (interface *a* or *a'*) is primarily mode II, whereas delamination into the thin region (interface *b*), is mostly mode I. Figure 22 shows a comparison of total G calculated by ANSYS and ABAQUS for delamination along interface *a'*. The results from the two codes agreed very well for all cases compared, when the details of the models were carefully matched in the codes. The figure also shows that the G

value reached an initial peak, dropped sharply, and then increased to another peak. As the figure indicates, the initial delamination growth was between two plies; however, as the delamination continued, growing between a ply and the resin pocket in front of the next dropped ply, G dropped. When the delamination was again between two plies, G increased to the second peak. Throughout this range of delamination, G along interface *a'* was at least 95% mode II.

Specimens of both types were tested under cyclic loading in the ATB. The specimens were visually monitored periodically for delamination onset and growth. Delamination began at the same ply-drop location, ply-ending 311, for all the test specimens. Delaminations then grew toward the thick end of the laminate, initially along the interface toward the midplane (*a'*), and then also along the interface toward the surface (*a*). Figure 23 shows a representative photo of a delaminated flexbeam. In all cases, the delamination growth was slow and stable. Some tests were allowed to continue until delaminations had formed at multiple interfaces and grown extensively; however, none of the flexbeams with this ply-drop scheme failed catastrophically. Calculated surface strains along the length of the specimen also agreed very well with the measured strains for this configuration.

Calculated peak G values for each hybrid configuration were used with mode II fatigue data to calculate fatigue life curves for these flexbeams, using the method from ref. 18, and described above, using eqs. 1-4, and the appropriate relationships from the analyses and tests. Figure 24 shows the calculated life prediction curve for these specimens, along with the test data. The test results agree reasonably well with the calculated curves.

This fracture mechanics approach has been demonstrated to work well for other structural applications. In ref. 23, delamination in the flange region of hat stringer specimens was evaluated using FE modeling and a fracture mechanics approach similar to the one described here for tapered laminates. The details of the flange region were modeled to duplicate the as-manufactured microstructure. Calculated G results and a mixed-mode failure criterion were used to accurately predict the hat stringer pull-off loads. In ref. 24, a fatigue life methodology similar to that used in [18-20] was demonstrated for delamination in a tapered composite flange bonded to a composite skin. A 2D finite element model with a geometrically nonlinear analysis was used to simulate the delamination growth observed in test specimens. The peak G values were used with mixed-mode fatigue life data to create a fatigue life onset G vs. N curve for delamination. The results were in good agreement with the test data.

CONCLUDING REMARKS

A summary of several studies of delamination in tapered composite laminates with internal ply-drops was presented. Initial studies dealt with linear tapered laminates under tension loading. Both 2D finite element modeling and laboratory tests were used to evaluate delamination onset and growth. In later studies, nonlinear tapered specimens, which were cut from a full-size helicopter rotor hub, were tested under combined constant axial tension and cyclic transverse bending loading to simulate the loading experienced by a rotorhub flexbeam in flight. A 2D FE model was created that duplicated the test flexbeam layup, geometry, and loading. The delamination patterns observed in the tests were simulated in the model by releasing pairs of MPCs. Strain energy release rates associated with the delamination growth were calculated for several configurations and using two different FE analysis codes. The strain energy release rate results were used with material characterization data to predict fatigue delamination onset lives for nonlinear tapered flexbeams with two different ply-dropping schemes. Some results of these studies are:

1. Interlaminar normal stresses in linear tapered laminates showed sharp peaks at the dropped ply locations and juncture of the thin and tapered regions, for a variety of layups and materials modeled, indicating that those stress peaks are likely due to the tapered geometry and material discontinuity at the ply drops.
2. Calculated strain energy release rates for delamination in the linear tapered laminates indicated that delamination was most likely to grow from the juncture of thin and tapered regions toward the tapered region first and then continue in both directions in an unstable manner. Tests confirmed this behavior.
3. Simple 2D models can be used to accurately reproduce the global behavior of nonlinear tapered laminates under combined tension-bending loading.
4. Delamination in nonlinear tapered laminates under combined constant tension-cyclic bending loading began at the ply drop nearest the surface of the flexbeam and initially grew toward the tapered region, at the interfaces around the dropped ply region, in a stable manner. Under continued loading, some specimens failed catastrophically, delaminating along the entire length. Flexbeams with an alternative ply-drop scheme continued to delaminate at multiple interfaces, but without catastrophic failure.
5. Strain energy release rates associated with simulated delamination growth were calculated using the Virtual Crack Closure Technique. Delamination toward the tapered region was primarily mode II, and delamination toward the thin region was primarily mode I. Peak values of the calculated strain energy release rates were used with fatigue material characterization data to calculate fatigue life prediction curves for a variety of taper designs, material systems and ply-dropping schemes. Test data compared well with the predicted curves.

REFERENCES

1. Hoa, S. V., Daost, J., Du, B. L., and Vu-Khanh, T., "Interlaminar Stresses in Tapered Laminates," *Polymer Composites*, Vol. 9, (5), Oct 1988, pp. 337-344.
2. Daoust, J. and Hoa, S. V., "Parameters Affecting Interlaminar Stresses in Tapered Laminates Under Static Loading Conditions," *Polymer Composites*, Vol. 10, (5), Oct. 1989, pp. 374-383.
3. Kemp, B. L. and Johnson, E. R., "Response and Failure Analysis of a Graphite-Epoxy Laminate Containing Terminating Internal Plies." *Proceedings of the 26th AIAA/ASME/ASCE/AHS Structures, Structural Dynamics and Materials (SDM) Conference*, Orlando, FL, April 1985.
4. Curry, J. M., Johnson, E. R., and Starnes, J. H., "Effect of Dropped Plies on the Strength of Graphite-Epoxy Laminates," *Proceedings of the 29 th AIAA/ASME/ASCE/AHS Structures, Structural Dynamics and Materials (SDM) Conference*, Monterey, CA, April 1987.
5. Fish, J. C. and Lee, S. W., "Delamination of Tapered Composite Structures," Engineering Fracture Mechanics, Vol. 34, (1), 1989.
6. Ganesan, R., He, K., and Hoa, S. V., "Interlaminar Fracture Behavior of Internally Tapered Composite Laminates," Paper 138, *Proceedings of the American Society for Composites, 17th Technical Conference*, West Lafayette, IN, October, 2002.
7. Vidyashankar, B. R.and Krishna Murty, A. V., "Analysis of laminates with ply drops," *Composites Science and Technology*, 61, 2001, pp. 749-758.
8. Shim, D.-J. and Lagace, P. A., "Mechanisms and Structural Parameters Affecting the Interlaminar Stress Field in Laminates with Ply Dropoffs," Paper 039, *Proceedings of the American Society for Composites, 17th Technical Conference*, West Lafayette, IN, October, 2002.
9. Wisnom, M. R., "Delamination in Tapered Unidirectional Glass Fibre-Epoxy Under Static Tension Loading," *Proceedings of the32nd AIAA/ASME/ASCE/AHS Structures, Structural Dynamics and Materials (SDM) Conference (Part 2)*, Baltimore, MD, April, 1991.
10. Threthewey, B. R., Jr., Gillespie, J. W., Jr., and Wilkins, D. J., "Interlaminar Performance of Tapered Composite Laminates," *Proceedings of the American Society for Composites, 5th Technical Conference*, East Lansing, MI, June 1990.

11. Armanios, E. A. and Parnas, L., “Delamination Analysis of Tapered Laminated Composites Under Tensile Loading,” *Composite Materials: Fatigue and Fracture (Third Volume) ASTM STP 1110*, T. K. O’Brien, Ed., American Society for Testing and Materials, Philadelphia, PA, 1991.
12. O’Brien, T. K., “Towards a Damage Tolerance Philosophy for Composite Materials and Structures,” *Composite Materials: Testing and Design, Vol. 9, ASTM STP 1059*, S. P. Garbo, Ed., American Society for Testing and Materials, Philadelphia, 1990, pp. 7-33.
13. Salpekar, S. A., Raju, I. S., and O'Brien, T. K., "Strain Energy Release Rate Analysis of Delamination in a Tapered Laminate Subjected to Tension Load," *Proceedings of the American Society for Composites, Third Technical Conference*, Seattle, WA, Sept. 1988, pp. 642-654.
14. Murri, G. B., Salpekar, S. A., and O'Brien, T. K., "Fatigue Delamination Onset Prediction in Unidirectional Tapered Laminates," *Composite Materials: Fatigue and Fracture (Third Volume), ASTM STP 1110*, T. K. O'Brien, Ed., American Society for Testing and Materials, Philadelphia, 1991, pp. 312-339.
15. Murri, G. B., O'Brien, T. K., and Salpekar, S. A., "Tension Fatigue of Glass/Epoxy and Graphite/Epoxy Tapered Laminates," *Journal of the American Helicopter Society*, Vol. 38, No. 1, Jan. 1993, pp. 29-37.
16. Rybicki, E. F. and Kanninen, M. F., "A Finite Element Calculation of Stress Intensity Factors by a Modified Crack Closure Integral," *Engineering Fracture Mechanics*, Vol. 9, 1977, pp. 931-938.
17. Gardner, M. R., Young, R. S., and O’Brien, T. K., “Testing Machine Exerts Longitudinal and Transverse Loads”, NASA Tech Brief, 1993, 15.
18. Murri, G. B., O’Brien, T. K., and Rousseau, C. Q., "Fatigue Life Methodology for Tapered Composite Flexbeam Laminates," *Journal of the American Helicopter Society*, Vol. 43, No. 2, April 1998, pp. 146-155.
19. Murri, G.B., Schaff, J.R., and Dobyns, A. L., “Fatigue and Damage Tolerance of a Hybrid Composite Tapered Flexbeam,” Proceedings of the American Helicopter Society, Forum 54, Washington, D.C., May 2001.
20. Murri, G.B., Schaff, J.R., and Dobyns, A. L., “Fatigue Life Analysis of Tapered Hybrid Composite Flexbeams,” Proceedings of the 14 International Conference on Composite Materials (ICCM14), San Diego, CA, July 2003.
21. Martin, R. H. and O’Brien, T. K., “Characterizing Mode I Fatigue Delamination of Composite Materials,” 4th Technical Conference of the American Society for Composites, Blacksburg, Virginia, October 1989, pp. 257-266.
22. Martin, R. H., Interlaminar Fracture Characterization: A Current Review, NASA CR-187573.

23. Li, J., O'Brien, T. K., and Rousseau, C. Q., "Test and Analysis of Composite Hat Stringer Pull-off Test Specimens," *Journal of the American Helicopter Society*, October, 1997, pp. 350-357.

24. Krueger, R., Paris, I. L., O'Brien, T. K., and Minguet, P. J., "Fatigue Life Methodology for Bonded Composite Skin/Stringer Configurations," *Journal of Composites Technology and Research*, vol. 24, pp. 56-79, 2002.

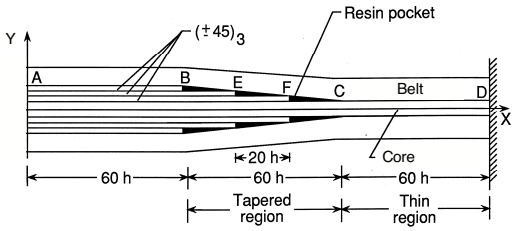

Figure 1. Schematic of tapered laminate with internal ply drops.

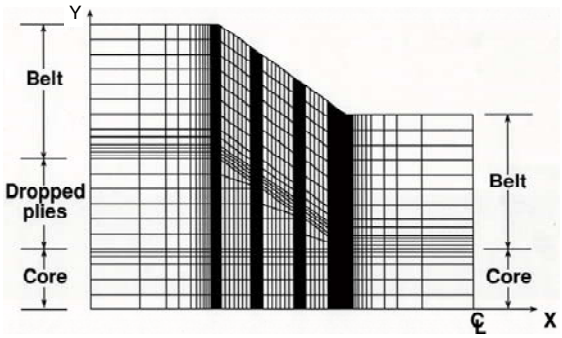

Figure 2. Finite element mesh of half-laminate.

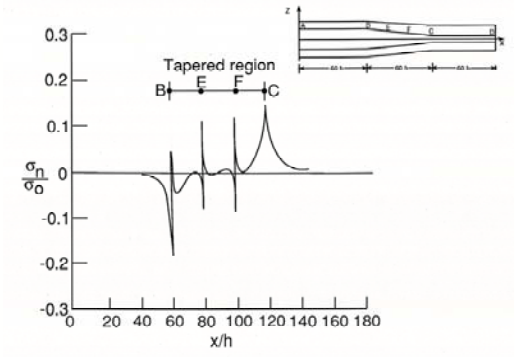

Figure 3. Interlaminar normal stresses in linear tapered laminate at interface ABCD.

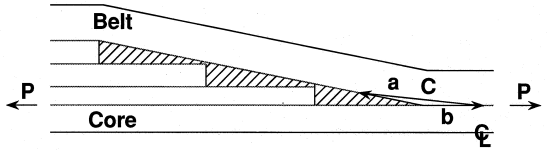

(a) Unstable delamination

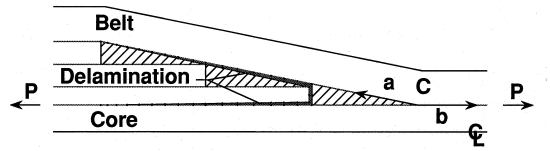

(b) Initial stable delamination

Figure 4. Delamination from point C, with and without initial delamination around dropped ply group.

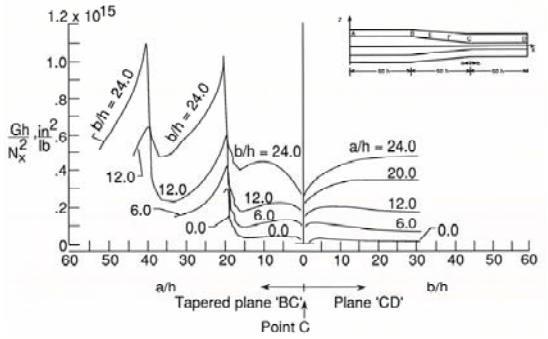

Figure 5. Strain energy release rates for delamination growth along BC or CD.

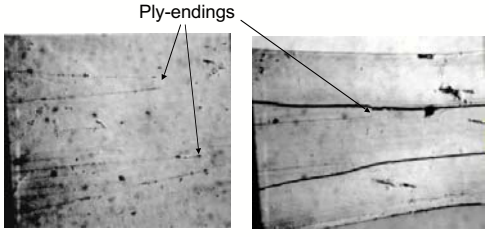

Figure 6. Initial delamination damage around ply ending and unstable delamination in tapered laminate.

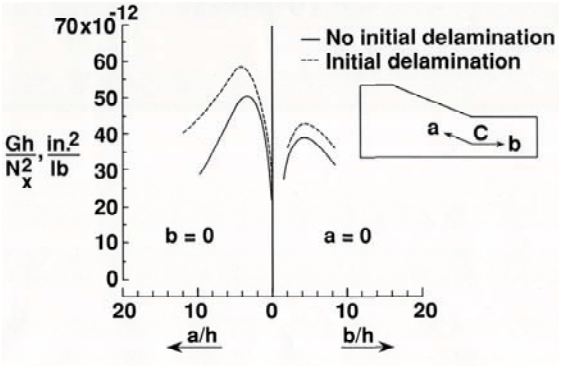

Figure 7. Strain energy release rates with and without initial delamination damage modeled.

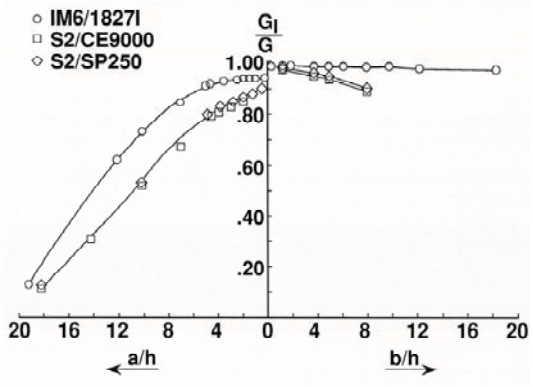

Figure 8. Mode I percentage of G for delamination growth into the tapered or thin regions.

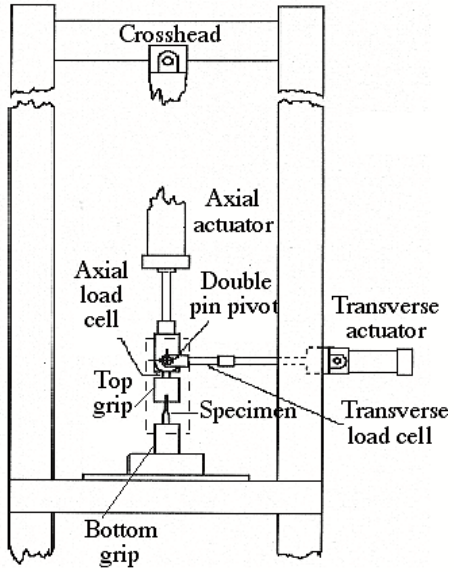

Figure 9. Schematic of the Axial-Tension and Bending (ATB) test stand.

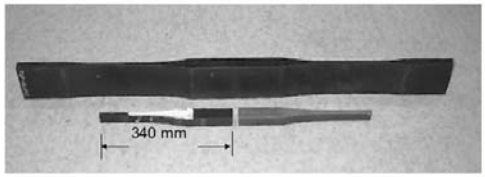

Figure 10. Flexbeam specimens cut from full-size rotorhub flexbeam.

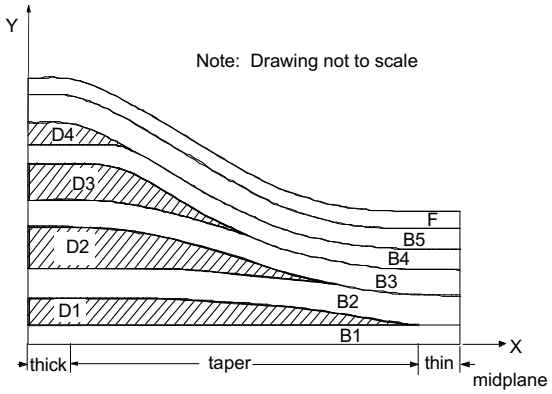

Figure 11. Schematic of cross-section of tapered flexbeam showing belt and dropped-ply groups.

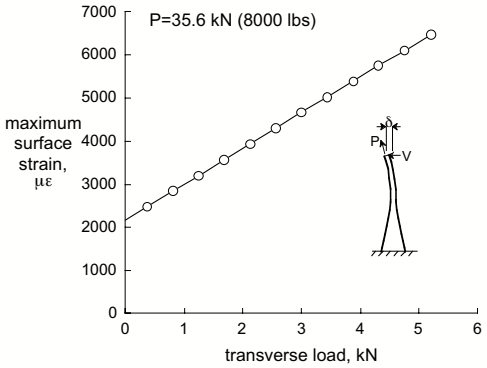

Figure 12. Surface strain vs. applied transverse load in tapered flexbeam with axial tension load.

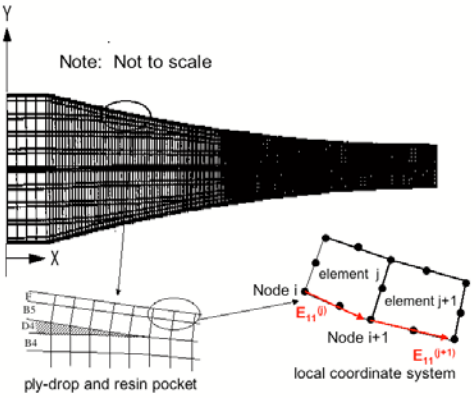

Figure 13. Finite element model of nonlinear tapered flexbeam.

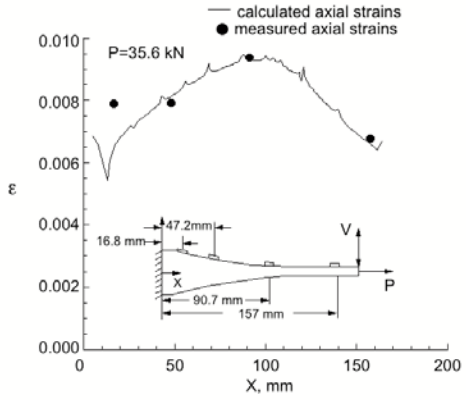

Figure 14. Surface strains in nonlinear tapered flexbeam with combined tension and bending loading.

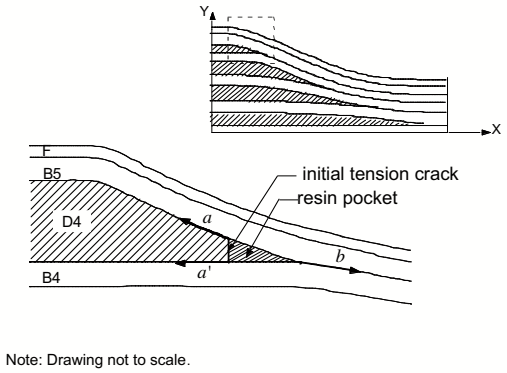

Note: Drawing not to scale.

Figure. 15. Delamination starting at tip of dropped ply and growing in 3 interfaces.

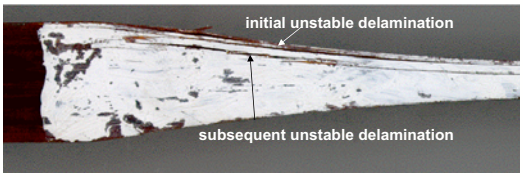

(a)Final unstable delamination at multiple interfaces.

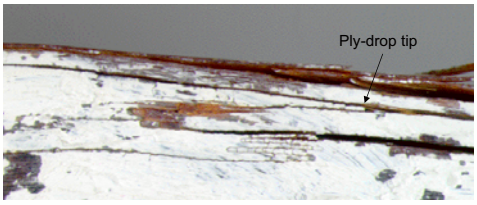

(b) Detail of delamination around ply-drop tip.

Figure 16. Delaminated flexbeam specimen.

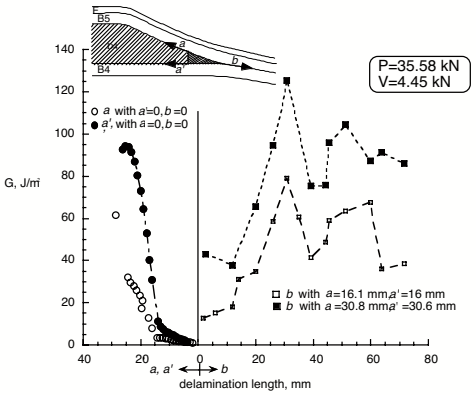

Figure 17. Strain energy release rates calculated from nonlinear tapered flexbeam model.

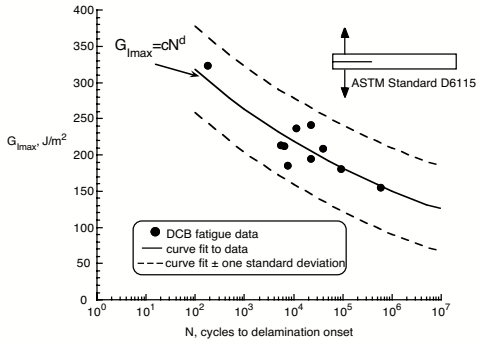

Figure 18. Fatigue delamination onset data from cyclic DCB specimens.

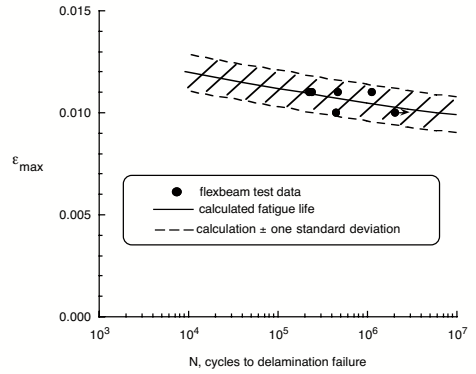

Figure 19. Predicted and measured fatigue life of nonlinear tapered composite flexbeams.

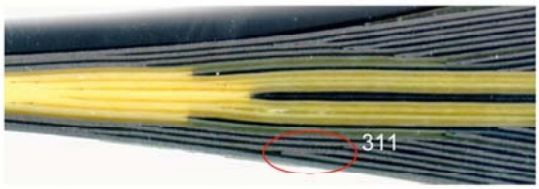

Figure 20. Edge view of glass/graphite hybrid flexbeam specimen.

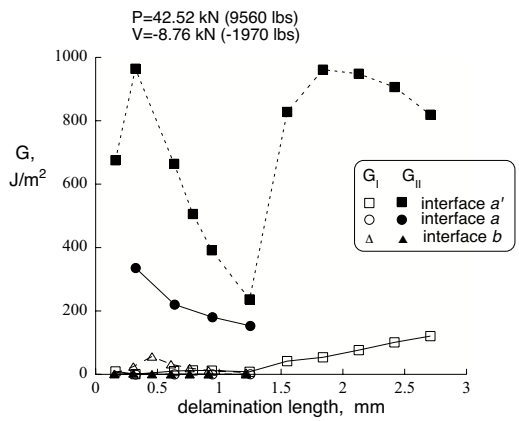

Figure 21. Strain energy release rates for delamination along three possible interfaces.

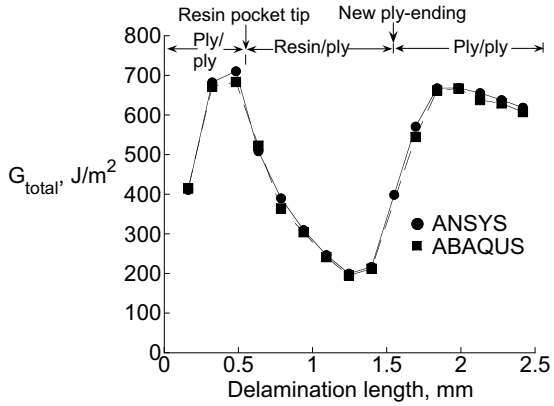

Figure 22. Comparison of ABAQUS and ANSYS strain energy release rates for delamination along interface a' in hybrid nonlinear tapered flexbeam.

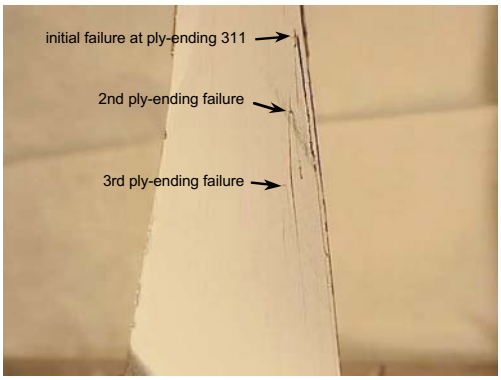

Figure 23. Typical delamination damage in hybrid nonlinear flexbeam.

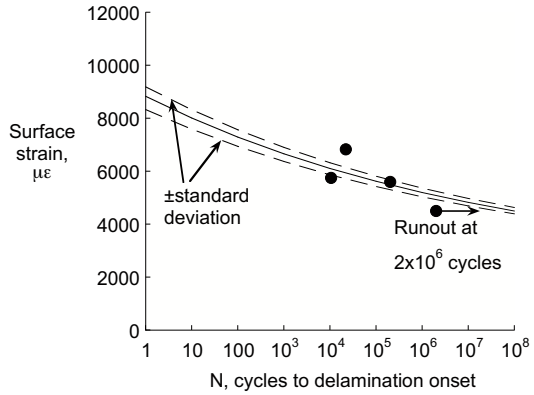

Figure 24. Fatigue life prediction and test results for graphite/glass hybrid nonlinear tapered flexbeam.